Research Article | Vol. 25, No. 21 | 16 Oct 2017 | OPTICS EXPRESS 25831

Optics EXPRESS

# Quantum dot emission modulation using piezoelectric photonic crystal MEMS resonators

GLORIA G SEE,[1] ANMING GAO,[1] LU XU,[2] RALPH NUZZO,[2] SONGBIN GONG,[1] AND BRIAN T. CUNNINGHAM[1,3,*]

[1]*Department of Electrical and Computer Engineering, University of Illinois at Urbana-Champaign, Micro and Nanotechnology Laboratory, 208 North Wright Street, Urbana, IL, 61801 USA*
[2]*Department of Chemistry, University of Illinois at Urbana-Champaign, 600 South Mathews Avenue, Urbana, Illinois 61801 USA*
[3]*Department of Bioengineering, University of Illinois at Urbana-Champaign, 1270 Digital Computer Laboratory, MC-278, Urbana, IL 61801 USA*
**bcunning@illinois.edu*

**Abstract:** Quantum dots (QDs) integration into photonic devices requires varied approaches to control and modulate their emission. We demonstrate voltage-tunable PC structures with integrated QDs over suspended piezoelectric aluminum nitride thin film resonators that modulate PC enhancement at MHz frequencies. When the piezoelectric device is actuated at its resonant mechanical frequency, the extracted QD emission direction is likewise modulated via the optical resonant frequency of the PC. Modulation uses nanometer-scale mechanical displacements, offering the potential for greater switching speed and improved mechanical robustness that is not subject to the effects of stiction with a scalable fabrication approach.



**OCIS codes:** (050.5298) Photonic crystals; (250.5590) Quantum-well, -wire and -dot devices; (250.4110) Modulators.

## References and links

1. J. Kwak, W. K. Bae, D. Lee, I. Park, J. Lim, M. Park, H. Cho, H. Woo, D. Y. Yoon, K. Char, S. Lee, and C. Lee, "Bright and efficient full-color colloidal quantum dot light-emitting diodes using an inverted device structure," Nano Lett. **12**(5), 2362–2366 (2012).
2. H. Volkan, S. Nizamoglu, T. Erdem, E. Mutlugun, N. Gaponik, and A. Eychmüller, "Quantum dot integrated LEDs using photonic and excitonic color conversion," Nano Today **6**, 632–647 (2011).
3. A. Rahmani, A. Rostami, H. R. Saghai, and M. K. Moravvej-farshi, "Optik Ultrafast GaN / AlN modulator based on quantum dot for terabit all-optical communication," Optik (Stuttg.) **125**, 3844–3851 (2014).
4. B. S. Mashford, M. Stevenson, Z. Popovic, C. Hamilton, Z. Zhou, C. Breen, J. Steckel, V. Bulovic, M. Bawendi, S. Coe-sullivan, and P. T. Kazlas, "High-efficiency quantum-dot light-emitting devices with enhanced charge injection," Nat. Photonics **7**, 407–412 (2013).
5. K.-S. Cho, E. K. Lee, W.-J. Joo, E. Jang, T.-H. Kim, S. J. Lee, S.-J. Kwon, J. Y. Han, B.-K. Kim, B. L. Choi, and J. M. Kim, "High-performance crosslinked colloidal quantum-dot light-emitting diodes," Nat. Photonics **3**, 341–345 (2009).
6. Z. Zhou, B. Yin, and J. Michel, "On-chip light sources for silicon photonics," Light Sci. Appl. **4**, 1–13 (2015).
7. N. Yamamoto, K. Akahane, T. Umezawa, and T. Kawanishi, "Monolithically integrated quantum dot optical modulator with semiconductor optical amplifier for short-range optical communications," Jpn. J. Appl. Phys. **54**, 04DG01 (2015).
8. C. Y. Ngo, S. F. Yoon, W. K. Loke, Q. Cao, D. R. Lim, V. Wong, Y. K. Sim, and S. J. Chua, "Characteristics of 1.3 μm InAs/InGaAs/GaAs quantum dot electroabsorption modulator," Appl. Phys. Lett. **94**, 143108 (2009).
9. S. Weiss, M. C. Schlamp, and A. P. Alivisatos, "Electronic Displays Using Optically Pumped Semiconductor Nanocrystals," U.S. patent 6,864,626 B1 (2005).
10. C. E. Rowland, K. Susumu, M. H. Stewart, E. Oh, A. J. Mäkinen, T. J. O'Shaughnessy, G. Kushto, M. A. Wolak, J. S. Erickson, A. L. Efros, A. L. Huston, and J. B. Delehanty, "Electric Field Modulation of Semiconductor Quantum Dot Photoluminescence: Insights Into the Design of Robust Voltage-Sensitive Cellular Imaging Probes," Nano Lett. **15**(10), 6848–6854 (2015).
11. J. L. O'Brien, "Optical Quantum Computing," Science **318**(5856), 1567–1570 (2007).
12. A. Majumdar, N. Manquest, and A. Faraon, "Theory of electro-optic modulation via a quantum dot coupled to a nano-resonator," Opt. Express **18**, 18651–18658 (2010).
13. W. Liu, R. S. Kim, B. Liang, D. L. Huffaker, and H. R. Fetterman, "High-Speed InAs Quantum-Dot Electrooptic

#304497 https://doi.org/10.1364/OE.25.025831
Journal © 2017 Received 9 Aug 2017; revised 1 Oct 2017; accepted 2 Oct 2017; published 10 Oct 2017

Optics EXPRESS

Phase Modulators," IEEE Photonics Technol. Lett. **23**, 1748–1750 (2011).
14. X. Yang, K. Dev, J. Wang, E. Mutlugun, C. Dang, Y. Zhao, S. Liu, Y. Tang, S. T. Tan, X. W. Sun, and H. V. Demir, "Light Extraction Efficiency Enhancement of Colloidal Quantum Dot Light-Emitting Diodes Using Large-Scale Nanopillar Arrays," Adv. Funct. Mater. **24**, 5977–5984 (2014).
15. S. R. K. Rodriguez, G. Lozano, M. A. Verschuuren, R. Gomes, K. Lambert, B. De Geyter, A. Hassinen, D. Van Thourhout, Z. Hens, and J. G. Rivas, "Quantum rod emission coupled to plasmonic lattice resonances: A collective directional source of polarized light," Appl. Phys. Lett. **100**, 111103 (2012).
16. M. Davanço, M. T. Rakher, D. Schuh, A. Badolato, and K. Srinivasan, "A circular dielectric grating for vertical extraction of single quantum dot emission," Appl. Phys. Lett. **99**, 041102 (2011).
17. P. Lodahl, A. Floris Van Driel, I. S. Nikolaev, A. Irman, K. Overgaag, D. Vanmaekelbergh, and W. L. Vos, "Controlling the dynamics of spontaneous emission from quantum dots by photonic crystals," Nature **430**(7000), 654–657 (2004).
18. G. G. See, L. Xu, M. S. Naughton, T. Tang, Y. Bonita, J. Joo, P. Trefonas, K. Deshpande, P. J. Kenis, R. G. Nuzzo, and B. T. Cunningham, "Region specific enhancement of quantum dot emission using interleaved two-dimensional photonic crystals," Appl. Opt. **54**(9), 2302–2308 (2015).
19. N. Ganesh, W. Zhang, P. C. Mathias, E. Chow, J. A. N. T. Soares, V. Malyarchuk, A. D. Smith, and B. T. Cunningham, "Enhanced fluorescence emission from quantum dots on a photonic crystal surface," Nat. Nanotechnol. **2**(8), 515–520 (2007).
20. K. McGroddy, A. David, E. Matioli, M. Iza, S. Nakamura, S. Denbaars, J. S. Speck, C. Weisbuch, and E. L. Hu, "Directional emission control and increased light extraction in GaN photonic crystal light emitting diodes," Appl. Phys. Lett. **93**, 103502 (2008).
21. M. Rippa, R. Capasso, P. Mormile, S. De Nicola, M. Zanella, L. Manna, G. Nenna, and L. Petti, "Bragg extraction of light in 2D photonic Thue-Morse quasicrystals patterned in active CdSe/CdS nanorod-polymer nanocomposites," Nanoscale **5**(1), 331–336 (2013).
22. N. Ganesh, P. C. Mathias, W. Zhang, and B. T. Cunningham, "Distance dependence of fluorescence enhancement from photonic crystal surfaces," J. Appl. Phys. **103**, 083104 (2008).
23. L. Xu, E. Sutanto, A. G. Alleyne, R. G. Nuzzo, and B. T. Cunningham, "Polarized quantum dot emission in electrohydrodynamic jet printed photonic crystals," Appl. Phys. Lett. **107**, 051101 (2015).
24. Y. Shimoda, M. Ozaki, and K. Yoshino, "Electric field tuning of a stop band in a reflection spectrum of synthetic opal infiltrated with nematic liquid crystal," Appl. Phys. Lett. **79**, 3627–3629 (2001).
25. M. Haurylau, S. P. Anderson, K. L. Marshall, and P. M. Fauchet, "Electrical modulation of silicon-based two-dimensional photonic bandgap structures," Appl. Phys. Lett. **88**, 2172070 (2006).
26. Y. Saado, M. Golosovsky, D. Davidov, and A. Frenkel, "Tunable photonic band gap in self-assembled clusters of floating magnetic particles," Phys. Rev. B **66**, 195108 (2002).
27. H. Tian and J. Zi, "One-dimensional tunable photonic crystals by means of external magnetic fields," Opt. Commun. **252**, 321–328 (2005).
28. D. Englund, A. Faraon, A. Majumdar, N. Stoltz, P. Petroff, and J. Vuckovic, "An optical modulator based on a single strongly coupled quantum dot-cavity system in a p-i-n junction," Opt. Express **17**(21), 18651–18658 (2009).
29. Y. H. Cui, Q. Wu, W. Park, J. Jeon, M. J. Kim, and J. B. Lee, "MEMS-based mechanically tunable flexible photonic crystal," in *TRANSDUCERS 2009 - 15th International Conference on Solid-State Sensors, Actuators and Microsystems* (IEEE, 2009), pp. 509–512.
30. S. Kim and V. Gopalan, "Strain-tunable photonic band gap crystals," Appl. Phys. Lett. **78**, 3015–3017 (2001).
31. I. R. Howell, C. Li, N. S. Colella, K. Ito, and J. J. Watkins, "Strain-Tunable One Dimensional Photonic Crystals Based on Zirconium Dioxide/Slide-Ring Elastomer Nanocomposites for Mechanochromic Sensing," ACS Appl. Mater. Interfaces **7**(6), 3641–3646 (2015).
32. O. Levy, B. Z. Steinberg, A. Boag, S. Krylov, and I. Goldfarb, "Mechanical tuning of two-dimensional photonic crystal cavity by micro Electro mechanical flexures," Sens. Actuators A Phys. **139**, 47–52 (2007).
33. S. Jun and Y.-S. Cho, "Deformation-induced bandgap tuning of 2D silicon-based photonic crystals," Opt. Express **11**(21), 2769–2774 (2003).
34. Q. Wang, E. T. F. Rogers, B. Gholipour, C.-M. Wang, G. Yuan, J. Teng, and N. I. Zheludev, "Optically reconfigurable metasurfaces and photonic devices based on phase change materials," Nat. Photonics **10**, 60–65 (2015).
35. N. I. Zheludev and E. Plum, "Reconfigurable nanomechanical photonic metamaterials," Nat. Nanotechnol. **11**(1), 16–22 (2016).
36. S. Sun, H. Kim, G. S. Solomon, and E. Waks, "Strain tuning of a quantum dot strongly coupled to a photonic crystal cavity," Appl. Phys. Lett. **103**, 151102 (2013).
37. C. W. Wong, P. T. Rakich, S. G. Johnson, M. Qi, H. I. Smith, E. P. Ippen, C. Lionel, Y. Jeon, G. Barbastathis, and S. Kim, "Strain-tunable silicon photonic band gap microcavities in optical waveguides," Appl. Phys. Lett. **84**, 1242 (2004).
38. S. Krishnamurthy and P. V. Santos, "Optical modulation in photonic band gap structures by surface acoustic waves," J. Appl. Phys. **96**, 1803–1810 (2004).
39. G. N. Nielson, R. H. Olsson, P. R. Resnick, and O. B. Spahn, "High-speed MEMS micromirror switching," in *Conf. Lasers Electro-Optics, 2007 CLEO* (2007), pp. 2–3.
40. C. Duarte, E. Salm, B. Dorvel, B. Reddy, Jr., and R. Bashir, "On-chip parallel detection of foodborne pathogens

Optics EXPRESS

using loop-mediated isothermal amplification," Biomed. Microdevices **15**(5), 821–830 (2013).
41. R. Aigner, "MEMS in RF filter applications: Thin-film bulk acoustic wave technology," Sensors Updat. **12**, 175–210 (2003).
42. (Ferro-Ceramic Grinding Inc.), "Ceramic Properties Tables," http://ferroceramic.com/alumina_nitride_table.htm.
43. Q. D. Ubi, "UbiQD Announces Record Efficiency from its Cadmium-Free Quantum Dots," http://ubiqd.com/2017/04/10/ubiqd-announces-record-efficiency-cadmium-free-quantum-dots/.
44. D. Armitage, I. Underwood, and S. Wu, *Introduction to Microdisplays* (John Wiley & Sons, Inc, 2006).
45. DOE/Oak Ridge National Laboratory, "Large-scale techniquee to product quantum dots," www.sciencedaily.com/releases/2016/05/160519161227.htm.

## 1. Introduction

An increasing number of photonic devices contain integrated quantum dots (QDs), semiconductor nanoparticles that are efficiently excited by high energy photons, producing a lower energy output emission with a narrower bandwidth than phosphors, enabling improved gamut and color tuning of outputs [1,2] as well as reduced operating power and increased device speed [3]. However, due to the cost of producing high quality QDs, there is significant interest in increasing the efficiency of QD emission in devices and reducing the quantities required, while using the high brightness of QDs to reduce power requirements [2,4,5]. QD emission must be modulated for many applications, including telecommunications [6–8], displays [9], imaging [10], and quantum computing [11,12], with demonstrated QD modulation rates ranging from DC to GHz [12,13].

One method for controlling and enhancing QD emission is to incorporate them into nanostructures, such as nanopillars [14], plasmonic surfaces [15], gratings [16], and photonic crystals (PCs) [17–19]. PCs are dielectric nanostructures with periodic variation in their refractive index that can be designed to function as optical resonators at specific wavelengths, with the ability to couple energy into QDs at their excitation wavelength [18,19] and to channel QD emission in specific desired directions from the PC surface [20,21]. PC-enhanced excitation and extraction have been utilized for applications that include biosensing [22] and lighting [5], where increased brightness from photon emitters can be used to reduce limits of detection and to increase signal-to-noise ratios. Another useful feature of integrating QDs within PCs is emission extraction that is highly polarized, even when excited by a non-polarized excitation source, offering the potential to improve energy efficiency through elimination of linear polarization filters that currently block half of the emitted photons in a conventional video display from reaching the viewer [23].

In this work, we focus specifically upon PC-enhanced emission extraction, in which QD emitters within a PC will channel their output in a direction dictated by the PC dispersion, resulting in narrow bandwidth QD emission emerging from the PC along a specific and narrow band of exit angles. The observed brightness of QD emission emerging from a PC can be greater than that from QDs emitting from a planar surface because the emission that would ordinarily be isotropically distributed is channeled within a narrow beam.

While the majority of PCs are static structures, providing enhanced extraction characteristics that cannot be changed, several methods have been investigated to produce mechanically or optically tunable PC structures through adjustment of refractive index via application of external electric [24,25] or magnetic fields [26,27], including incorporating a PC into a P-I-N junction [28], or adjusting the PC period through mechanical stress [29–33]. Reconfigurable photonic structures have also been demonstrated with phase change materials [34] and nanomechanical metamaterials [35]. PCs have incorporated piezoelectric materials to enable voltage-tuned control of their resonance wavelength; however, prior reports of piezoelectrically-tuned PCs [36,37] require kV-scale voltages and significant wavelength tuning magnitudes, which makes device integration difficult. Additional methods for PC resonance tuning with piezoelectric materials have been modeled using computer simulation tools, but not experimentally demonstrated. For example, arrays of air holes upon a piezoelectric substrate [30], or surface-acoustic wave-excited Bragg stacks which utilize

Optics EXPRESS

modulation of the refractive index to control the reflection/transmission spectra of a structure under voltage control [38].

In this work, we demonstrate actively tunable PC structures with integrated QD emitters, enabling the enhanced extraction characteristics of a PC to be modulated at MHz frequencies by constructing a PC with integrated QD emitters upon a piezoelectrically actuated, mechanically resonating membrane. We demonstrate that when the device is actuated at its resonant mechanical frequency by integrated electrodes, the extracted QD emission direction is likewise modulated. The rapid and voltage-modulated directional switching is analogous to the function of a pixel within a digital micromirror display (DMD), in which a mechanical mirror pivots on torsion hinges and makes mechanical contact to landing points. Unlike DMD mirror switching, which requires micron-scale motion of the mirror to switch between states, our approach requires only tens of nanometer mechanical displacements to modulate output emission, and is not subject to stiction. The switching speeds of 40-85 nanoseconds are determined by the RF modulation frequency, as compared to a 225 ns DMD switching speed [39].

We explore the design space for a single pixel of a QD-integrated, piezoelectrically modulated PC display, where we consider the device support geometry and dimensions that determine the mechanical resonant frequency and required actuation voltage. We demonstrate, with support from finite element modeling, multiple device geometries that enable large PC dimension displacement with voltages under 5 V produced using a simple, robust microfabrication process that requires only four photolithography steps. We demonstrate voltage controlled modulation of the QD output, by collecting the pixel output into an optical fiber end facet. Importantly, modulation of the QD emission from an "on" to "off" state, in which "on" represents QD emission capture into the distal end of an optical fiber, is achieved with less than 100 nm of average mechanical surface displacement.

## 2. Materials and Methods

The device, shown in the cross-sectional schematic in Fig. 1(a), is based on a bulk acoustic wave (BAW) resonator. It consists of a 1 μm thick piezoelectric layer of aluminum nitride (AlN) sandwiched between 100 nm thick platinum electrodes. There is an additional 1 μm layer of AlN over the top electrode with a PC grating covered by a UV curable polymer, which encapsulates the QDs. The thin film stack is released from the substrate during fabrication by dry etching of the underlying silicon, as shown in the photograph in Fig. 1(b) and the SEM in Fig. 1(c), leaving it suspended over a cavity and free to resonate. Tethers at the device ends or corners mechanically anchor it to the substrate.

The BAW resonator designs were simulated using finite element analysis (Comsol Multiphysics 5.1, Piezoelectric module) to determine optimal device dimensions, tether configurations, and the corresponding RF frequencies at mechanical resonance to produce adequate displacement. Here, "displacement" refers to mechanical expansion or contraction across the surface of the resonator where the PC is located. In particular, lateral displacements perpendicular to the PC grating "teeth" will change the grating period, which is the primary factor that modulates the PC resonant wavelength.

A minimum mechanical displacement of 10 nm in the PC grating period on the pixel surface was estimated to cause a $\Delta\lambda$ = 15 nm shift in the photonic resonance wavelength, based on previous PC designs [23]. This mechanical surface displacement is enough to cause a detectable change in the extracted output direction of embedded QDs. Note that, because some regions of the MEMS platform do not undergo identical displacement, but QDs are applied uniformly over the platform, only a portion of the QD output will be modulated by this mechanism, and not all modulated QDs undergo the same magnitude of angle tuning. The mechanical resonator designs were evaluated by determining which devices had resonant frequencies that would provide an average surface displacement of greater than 10 nm at the surface of the top AlN layer, and thus in the PC grating.

Optics EXPRESS

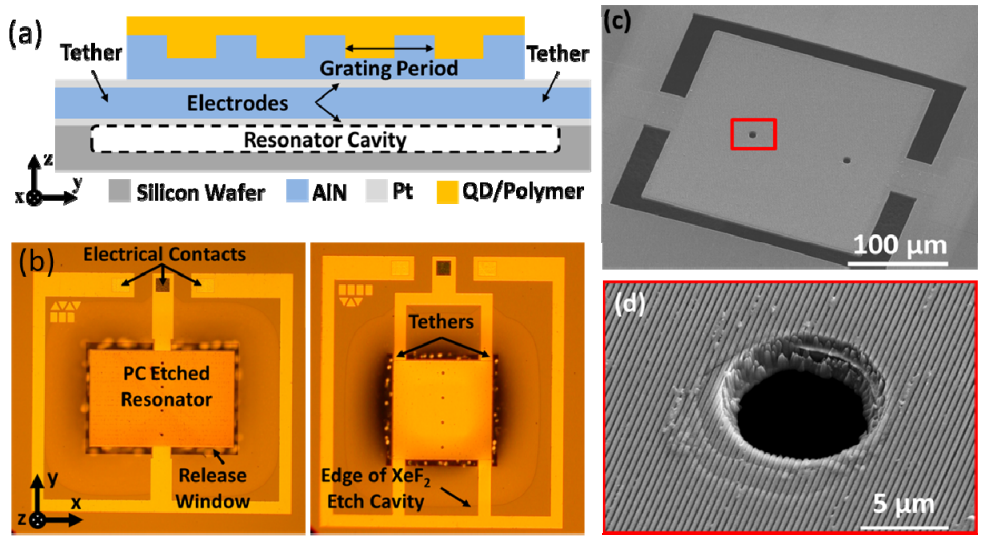


Fig. 1. Structure of the PC MEMS resonator: (a) A cross sectional schematic shows the device is suspended over a release cavity, and tethers connect the resonator to the substrate material. A piezoelectric AlN layer sandwiched between Pt electrodes, and covered by a PC grating in AlN with a printed layer of UV curable polymer and embedded QDs. (b) Photographs of two completed devices show the resonator body surrounded by the release windows for the two and four tether configurations. The resonators are suspended over a larger cavity, and supported by two or four tethers extending from the Pt layers. (c) An SEM of a resonator, with a higher resolution SEM (d) showing the PC grating structure around an etch via. The vias were used to decrease the release time.

The mechanical resonance of the structure was determined by plotting the frequency versus the admittance of each device, where a maximum in the admittance indicates a resonant frequency. The surface average function was then used to identify the resonant frequencies with the largest displacement value as an average across the entire resonator surface. A variety of pixel size dimensions ranging from 150 to 500 µm were simulated. The device dimensions selected for fabrication had a maximum surface displacement along the y-axis of the surface, orthogonal to the PC grating, shown in the SEM of the PC grating in Fig. 1(d).

Resonators with two tethers centered on opposite ends or four tethers (one on each corner) with the same resonator body dimensions were also simulated. These devices were included due to concerns that the multiple AlN layers would be too heavy to be supported by the dual tether design. A list of the devices that were simulated and fabricated, along with their modeled mechanical resonance frequencies and corresponding average displacement values, is shown in Table 1.

**Table 1. Key simulated and measured values for resonators[a]**

| L [µm] | W [µm] | Tethers | $f_r$* [MHz] | $\overline{D}$* [nm] | $f_r$† [MHz] | $Q$† | \|µV\| at $f_r$† |
|---|---|---|---|---|---|---|---|
| 225 | 150 | 2 | 31.61 | 47.87 | 28.78 | 872.02 | – |
| 225 | 225 | 2 | 22.79 | 86.82 | 21.49 | 364.69 | – |
| 400 | 300 | 2 | 15.99 | 103.71 | 14.64 | 518.06 | 20.71 |
| 400 | 300 | 4 | 14.65 | 104.90 | 14.47 | 72.85 | – |
| 400 | 350 | 2 | 14.05 | 116.80 | 12.65 | 327.57 | 16.72 |
| 400 | 400 | 2 | 12.81 | 128.37 | 11.52 | 148.42 | – |
| 400 | 450 | 2 | 11.14<br>30.78 | 149.79<br>12.77 | 11.02<br>29.25 | 61.88<br>199.72 | –<br>– |
| 500 | 350 | 2 | 13.60<br>26.29 | 100.77<br>15.99 | 12.21<br>23.86 | 369.99<br>512.49 | 18.65<br>47.19 |

Optics EXPRESS

| | | | | | | | |
|---|---|---|---|---|---|---|---|
| 500 | 400 | 2 | 12.09 | 139.32 | 11.26 | 228.13 | – |

[a]**L** is the resonator length, **W** is the resonator width, **D** is displacement, and $f_r$ is a resonant frequency. *Simulated value, †Measured value

The average surface displacement and admittance simulation results are shown in Fig. 2, where Fig. 2(a) and Fig. 2(b) are results for a 225 µm x 225 µm, two tether device and Fig. 2(c) and Fig. (d) are simulation results for a 450 µm x 400 µm, four tether device. Figure 2(a) and Fig. (c) are the plots of average surface displacement and admittance for the two device configurations, and show the maxima in the displacement correspond to the resonances indicated by the admittance. Figure 2(b) and Fig. (d) show the simulated displacements for the devices at different resonance frequencies. The two tether device simulation, Fig. 2(b), shows the largest displacement in the corners for the 22.78 MHz resonance. Devices with four tethers generally showed a greater displacement in the resonator center, such as is in the 30.79 MHz simulation in Fig. 2(d); however, devices with multiple resonance frequencies also showed increased displacement at the center of the resonator as mode patterns changed.

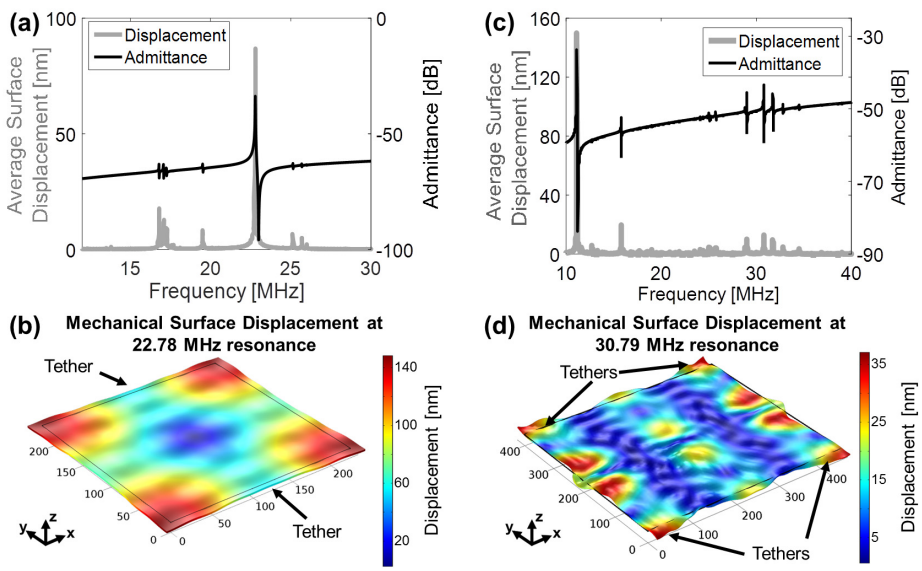


Fig. 2. Simulated admittance and the mechanical displacement averaged over the resonator surface for (a) a 225 µm x 225 µm, two tether device and (c) a 450 µm x 400 µm, four tether device. The peak average displacement values correspond to resonant frequencies indicated by maximum values in the admittance. (b) The simulated surface displacement at each point of the device surface on the same 225 µm x 225 µm, two tether device. The mechanical surface displacement is simulated at the resonant frequency 22.78 MHz, where the admittance and surface average displacement are at a maximum in (a). (d) The simulated surface displacement of the 450 µm x 400 µm, four tether device at its 30.79 MHz resonant frequency. The areas with the greatest displacement vary with size, tether position and frequency mode.

By adjusting the period of the PC grating etched into the top AlN layer, the resonant optical wavelength shifts and the magnitude of the electric field within the PC at that wavelength will decrease. The electric fields were determined using finite difference time domain simulations (Lumerical FDTD) for aluminum nitride (AlN) gratings covered by a layer of UV curable polymer with embedded CdSe quantum dots. Simulations were performed in which the PC is illuminated with broadband light at normal incidence to establish the resonant wavelength, at which an electromagnetic field standing wave with greater intensity than the illuminating field is established. As shown previously [19], the resonant wavelength at normal incidence corresponds to the QD emission wavelength that is extracted at normal exitance.

Optics EXPRESS

The QD emission is centered at λ = 540 nm with a full-width at half maximum of λ = 30 nm. The optimal design for PC enhanced extraction for a normal angle of exit at that wavelength consists of a 175 nm deep grating with a 350 nm period and a 600 nm thick polymer layer. A range of grating periods were simulated, as shown in Fig. 3, to confirm that the electric field at the QD emission wavelength for both increased and decreased surface displacements would be much lower than that of the "static" condition in the PC. The electric field intensity at λ = 538 nm decreases by 62-79%, depending on the displacement of the grating period. Therefore, the PC is designed to outcouple the QD emission at normal incidence when in its static state, and outcouple emission at a non-normal angle when the PC is under applied voltage that results in piezoelectric displacement temporarily modifying the PC grating period. Additional outcoupling angles were also simulated until the peak electric field intensity had decreased 63% (1/e) to 4.7 V/m at 19.8° to estimate the divergence of the PC output. The reflectivity of the electrode layers makes it difficult to measure the photonic bandgap of the PC.

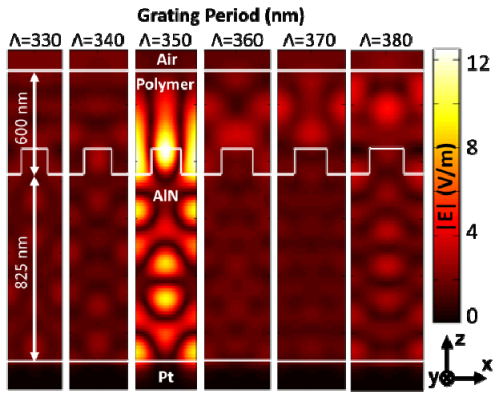


Fig. 3. The simulated electric field intensity at the center wavelength of the QD emission (λ = 538 nm) for varied grating periods. Increasing or decreasing the grating period by greater than 10 nm, reduces the electric field enhancement of the QD emission by 62-79%.

The fabrication process, illustrated in Fig. 4, was performed on a high resistivity silicon substrate. The bottom electrodes were evaporated onto the surface (CHA SEC-600 Electron Beam/Thermal Evaporator), and the AlN layer was reactively sputtered (OEM Group). The Pt/AlN layer deposition was repeated for the second electrode and the AlN PC layer.

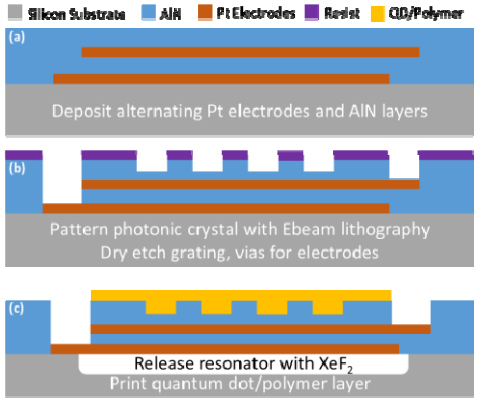


Fig. 4. A diagram of the fabrication process used to produce the PC MEMS devices. (a) Pt electrodes alternating with AlN layers were deposited on a high resistivity Si wafer. (b) The PC grating, electrical vias, and release windows were etched using reactive ion etching. (c)

Optics EXPRESS

Finally, the devices were released with XeF2 gas using the release windows, leaving the tethers to anchor the resonators to the substrate material, and then the suspended region was printed with a QD/polymer mix over the PC grating.

Electron beam lithography (JEOL JBX-6000FS) was used to pattern the PC grating, which was etched using inductively coupled plasma reactive ion etching (Oxford Instruments PlasmaLab System 100 ICP RIE) with a gas mix of $BCl_3$, $Cl_2$, and Ar in a 1:4:4 ratio. Photolithography was used to pattern the electrical vias and resonator release windows, which were separated into 1 µm and 2 µm deep features and etched using the same RIE process as for the PC grating.

After the AlN layer was removed from the Si wafer substrate to open the etch windows around the resonator bodies, the resonators were released with a $XeF_2$ etch (XACTIX $XeF_2$ Etching System). The release time varied with the size of the resonator; however, two tether devices with a width greater than 450 µm could not be released completely without collapsing the surrounding substrate. For four tether devices, the smaller release windows decreased this to a width of 300 µm.

A QD-doped polymer solution was prepared using two monomers, consisting of 91% Lauryl methacrylate (LMA, Sigma-Aldrich) and 9% ethylene glycol dimethacrylate (EGDMA, Sigma-Aldrich). CdSeS/ZnS alloyed QDs in a toluene solution (Sigma-Aldrich) were added, with the amount depending on the desired concentration of QDs. The remaining solvent was evaporated using a rotary evaporator and 1 v% Darocur 1173 (Sigma-Aldrich) initiator was added.

This QD/polymer solution was printed using a microinjector IM-300 (Narishige Scientific Instrument Lab. Tokyo, JP) that allowed for nL volumes to be dispensed [40] on the resonator surfaces. Finally, the QD/polymer layer was cured under a high intensity UV source for 30 minutes in an argon atmosphere glovebox to complete the devices. It is important to note that the printing takes place after the resonator release for optimal performance, as we discovered that the $XeF_2$ gas can permeate the cured polymer and subsequently etch the QDs, significantly reducing their emission intensity. Because of the devices lost to etching issues and $XeF_2$ release issues, the total device yield was 19%.

Completed devices were tested on an RF probe station. A network analyzer (Agilent N5230A PNA-L Network Analyzer) was used to sweep each device and determine the resonant frequencies at which to drive the devices. After characterization, a UV source (ThorLabs 370E UVLED) was passed through a 350 nm$<\lambda<$390 nm filter to eliminate any non-UV wavelengths, and the output was aligned onto the QD-printed resonator to excite QD emission. An optical fiber (400 µm, 0.39 NA) was mounted ~2 mm over the device under test, and aligned by adjusting position until the output measured by the connected photodetector (ThorLabs DET36) peaked. The output of the photodetector was measured by an oscilloscope (Agilent DSO 1614A). A signal generator (Agilent N5181A MXG Analog Signal Generator) was used to apply a signal at the mechanical resonant frequency. Using a splitter, this signal was also measured by an oscilloscope.

## 3. Results and Discussion

The PNA frequency sweep that determined the resonance conditions was compared to the modeled admittance characteristics. The sweep was performed at 1 dBm and 5 dBm to verify resonant frequencies would be consistent when operated with a higher driving power. The admittance characteristics changed slightly with power. The 5 dBm resonances had lower quality factors and often produced spurious modes at frequencies below 20 MHz, decreasing the performance of several devices.

The modeled admittance characteristics are compared with the measured values for all devices in Table 1, and an example plot of the modeled and measured admittance for a 400 µm x 300 µm, dual tether device is shown in Fig. 5. The measured resonance frequencies match the simulations within 1-2 MHz for devices with lengths less than 500 µm; however,

Optics EXPRESS

the quality factors are lower on the measured devices than in simulations due to slight misalignments during lithography steps, which caused non-uniform sidewalls, and residual strain in the AlN film. Larger devices showed a greater mismatch between the simulated and measured impedance values due to greater residual strain given their larger surface areas.

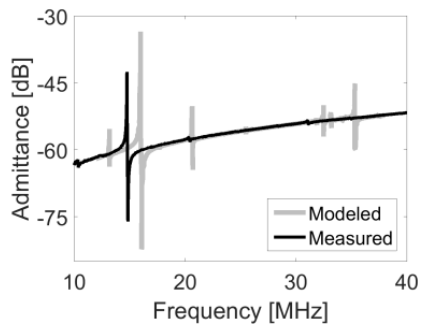


Fig. 5. A comparison of the modeled and measured impedance characteristics for a 400 µm x 300 µm device with two tethers. The quality factors of the measured impedances are lower than in the model, and thus not all resonance frequencies appear in the measured output. The measured peak admittance 14.64 MHz is 1.4 MHz offset from the simulated value of 15.99 MHz.

The four tether devices were found to have resonance characteristics (both frequency and displacement) that are comparable to two tether devices with the same dimensions for the resonator body. This is not a surprising result, since the resonant frequency for a BAW resonator is determined by the dimensions of the piezoelectric layer and the electrodes [41], since only the tether count and placement differs between those devices. The quality factors were dramatically lower on devices with four tethers, resulting from increased damping at the additional anchor points and the incomplete $XeF_2$ release.

When the resonant driving input was applied to each device, the measured QD emission of each device was compared to the driving RF signal and the output emission measured from the device with no RF modulation applied. During modulation, the outcoupling direction of the PC changes at the QD emission wavelength by at least 23°. This is the minimum angle change, as determined by the 400 µm core, 0.39 NA optical fiber located 2mm over the device surface, which shows the varied output emission intensity collected from the device by the optical fiber tip. Without the driving RF signal, the PC structure is static and the outcoupling of QD emitted light by the PC is constant.

An ideal device in the static state would have normal QD emission, ideally directed into the optical fiber for collection, and under oscillating input it would reach a minimum under both the compressive and tensile states. However, the applied PLMA film results in PC resonance wavelength that is not perfectly matched to the QD emission wavelength, and thus the QD emission in the zero-bias, or static condition is actually off-normal by an estimated five degrees, resulting in only one emission maxima per duty cycle.

The output emission signals had poor signal-to-noise ratios due to the short optical detection time possible on 10-30 MHz signals and the rise speed (14 ns) of the photodetector. To improve the quality of the optical output, the signals measured by the oscilloscope were averaged over 248-1024 measurements. Because of signal noise, a Fourier transform was performed on the measured signal data to confirm the modulated QD emission from the devices. This was seen when a peak in the Fourier transform of the output emission occurred at the same frequency as the RF input signal. The output modulation occurs at the same frequency as the mechanical resonance frequency of the devices, indicating modulation due to the modulated displacement. Thermal displacement was considered, but using 4.6 x10-6/°C as the thermal expansion coefficient of aluminum nitride [42], a temperate change of over 600 °C would be required for the 10 nm displacement to occur.

Optics EXPRESS

Figure 6 shows these measured results for a 500 µm x 350 µm device with two tethers, with the data integrated over 248 measurements. Figure 6(a) shows the integrated oscilloscope measurements of the outputs under both the static condition, and modulated at its 23.84 MHz resonance. The QD emission intensity varied with the driving voltage, but the intensity was constant and higher without the RF driving signal modulating the output. Figure 6(b) shows the Fourier transform applied to the same data (still integrated over 248 measurements) from the 500 µm x 350 µm device shown in Fig. 6(a). Figure 6(b) contains a peak at 23.84 MHz for the RF source and the modulated QD output from the device.

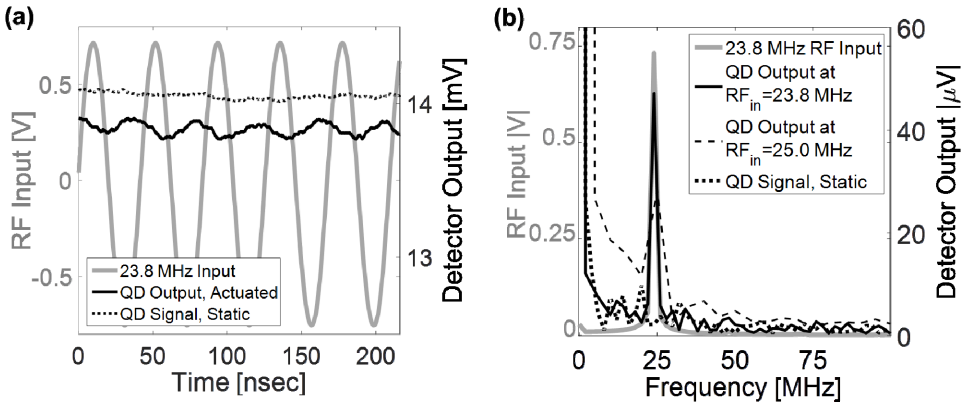


Fig. 6. (a) Measured oscilloscope signals from a 500 µm x 350 µm, two tether device. To improve signal to noise ratio, the data was integrated over 248 measurements. The QD emission output varies with the 23.9 MHz driving signal. When the driving signal is turned off, the emission is continuous. (b) A Fourier transform was applied to the time domain output signals of the RF source and the out-coupled QD emission while the device was actuated and static, integrated over 248 measurements. The QD emission from the device shows a peak at the same 23.9 MHz frequency of the resonant RF driving signal. The peak amplitude decreases as the input frequency is increased from the resonant frequency up to 25.0 MHz, while the DC component of the output emission increases. The peak is absent when the device is not actuated.

As the frequency of the RF input signal was increased, the power measured from the QD emission at the modulation frequency dropped sharply in the Fourier transform, the second peak shown in Fig. 6(b). This indicates that the mechanical displacement of the PC became less effective when the driving signal was changed from the acoustic resonance, and more of the QD emission was at DC than the modulated frequency. The device demonstrated this same behavior at its lower frequency resonance of 12.18 MHz, again with the power of the QD emission signal decreasing with a slight change of the modulation frequency.

As shown in Table 1, three device configurations showed strong modulation of the QD output emission. These all had a combination of high quality factor and large surface area. The smallest devices with high (>300) quality factors are expected to have strong modulation as well, but their smaller resonator area, and thus lower total QD emission, was insufficient to show distinguishable emission modulation with our test setup. No four tether devices showed effectively modulated outputs due to the lower quality factor at resonance.

## 4. Conclusions

The PC-MEMS hybrid devices presented in this paper leverage the enhancement mechanisms of PCs for improved QD emission, and have successfully demonstrated modulation of light emission from QDs embedded within the PC structure. The efficacy of the modulation is highly dependent on the dimensions of the resonator, affecting the uniformity of the PC displacement over the surface of the device, and the quality factor, which impacts the effective displacement.

Optics EXPRESS

This MHz-rate modulation of individual pixel devices could be applied across arrays of devices with red, green, and blue embedded QD emitters for active control of their aggregate emission in an electrically modulated QD video display, although the pixels would require isolation to avoid crosstalk between the driving RF signals.

This work reports on a novel modulation principle for photon emitters embedded within a mechanically modulated optical resonator. Applications will require mechanical resonator designs that are engineered for more uniform displacement over their surface, which may be achieved with more sophisticated tether architecture and platform shape. To improve integration of these devices into arrays, future devices would benefit from smaller release areas for better integration with existing display architecture, and we anticipate that scaling of devices to dimensions as small as 10x10 $\mu m^2$ will be achievable with available lithography capabilities. Integrating pixels into arrays would also be an opportunity to optimize the 1 dBm driving power utilized in this demonstration.

In addition, printing the QD-polymer mix over only the highest displacement regions of the PC would provide narrower angular output of the QD emission, and improve the on/off contrast for viewers. This improvement could also be produced using a DC biased device with more uniform surface displacement, though this approach requires more exotic piezoelectric materials with larger displacement coefficients. With improved contrast combined with QD optical efficiencies that can exceed 80% [43], the optical performance of PC-MEMS pixels would be competitive with that of existing display technologies such as LCDs, with an optical efficiency of 5-7% and DMDs with a throughput efficiency of ~60% [44].

The demonstration of MHz-rate modulation of PC-MEMS resonators has the potential to offer pixel level control of output emission in display devices with scalable CMOS compatible fabrication methods already used for DMDs and the thin-film transistors in LCDs in existing display technologies. This would enable competitive manufacturing costs as the production cost of QDs continues to decrease [45]. This approach utilizes a mechanically released device structure whose displacement does not result in contact with other surfaces, and is thus not subject to stiction forces. It requires low actuation voltages that generate nanometer-scale displacements, yet results in substantial angle tuning of the QD light emission for QD emission modulation.

## Funding

The Dow Chemical Company (226772AC).